Journal of Electronic Materials (2024) 53:4111–4119
https://doi.org/10.1007/s11664-024-10996-z

ORIGINAL RESEARCH ARTICLE

# Thermoelectric Properties of $Sb_2Te_3$ Ink Fabricated by Screen-Printing Technique

**Surasak Ruamruk[1,3] · Bralee Chayasombat[2] · Kunchit Singsoog[3] · Tosawat Seetawan[1]**

Received: 4 November 2023 / Accepted: 19 February 2024 / Published online: 29 April 2024


## Abstract

$Sb_2Te_3$-based thermoelectric (TE) ink was synthesized by mixing different $Sb_2Te_3$ microsizes with a ChaM-based solution. A thick-film TE was fabricated via a screen-printing technique on $SiO_2$/Si-wafer substrates. The thickness of the film was controlled at 200 $\mu$m, the film was dried on hotplates at 433 K for 30 min, and the film was annealed at 523 K under vacuum for 30 min. The crystal structure, morphology, chemical composition, Seebeck coefficient, electrical resistivity, thermal conductivity, and *ZT* were evaluated for the annealed film samples. The small powder size of $Sb_2Te_3$ was found to be in good condition, and a maximum *ZT* value of 1.04 was obtained at 468 K, which is more than three times that of the large size at the same temperature.

**Keywords** Thermoelectric ink · $Sb_2Te_3$ powder size · screen-printing technique · *ZT*

## Introduction

Currently, inorganic thermoelectric ink (TE) materials are widely used for their outstanding energy conversion capability, especially in thin-film or thick-film forms.[1] Several methods for the production of metal chalcogenide films have been developed.[2] Among these, the chalcogennidometalat (ChaM) method is known for its rich coordination chemistry, superior semiconducting behavior, and strong binding affinity to heavy metal ions.[3] The nanoscale semiconductor particles obtained using ChaM ions as precursors are widely utilized as inorganic ligands and solders. Molecular antimony telluride ($Sb_2Te_3$)-based ChaMs are used as a solder or a sintering aid for TE particles. $Sb_2Te_3$-ChaM easily fills the voids and interfaces between these TE particles.[4] The performance of TE materials is related to a parameter called the dimensionless figure-of-merit: $ZT = S^2T/\rho k = (\mathrm{PF})T/k$ where the Seebeck coefficient ($S$), electrical resistivity ($\rho$), thermal conductivity ($\kappa$), and absolute temperature ($T$).[5–7] $S^2/\rho$ are together typically called the power factor (PF).[8] Therefore, TE materials should simultaneously possess a high Seebeck coefficient and low electrical resistivity.[9] Among the numerous TE materials that have been developed[10] , $Sb_2Te_3$-based compounds are predominantly used as *p*-type TE materials for applications at room temperature because of their excellent TE properties in those ranges.[11] $Sb_2Te_3$-based TE films have been fabricated using different processes, such as printing,[12] spin-coating,[13] or screen-printing techniques.[14] The screen-printing technique was introduced for the fabrication of TE films because of its simplicity in processing and ease in thickness control.[15] Hyeongdo et al. reported the TE properties of screen-printed $Bi_{0.5}Sb_{1.5}Te_3$ and $Bi_2Te_{2.7}Se_{0.3}$ thick films using a post-annealing process with mechanical pressure. The $Bi_{0.5}Sb_{1.5}Te_3$ thick film had a *ZT* of 0.89 at room temperature.[16] Seong et al. reported a TE generator fabricated by multimaterial 3D printing of composition-segmented BiSbTe materials, by sequential deposition of all-inorganic viscoelastic TE inks. The maximum *ZT* of 3D-printed materials is 0.9 at 125°C.[17] Sung et al. reported high-performance shape-engineerable TE painting using the $Sb_2Te_3$ ChaM sintering process, effective even at 350 °C,

✉ Tosawat Seetawan
t_seetawan@snru.ac.th

1 Program of Physics, Faculty of Science and Technology, Sakon Nakhon Rajabhat University, 680 Nittayo Road, Mueang District, Sakon Nakhon 47000, Thailand

2 National Metal and Materials Technology Center (MTEC) Thailand Science Park, Khlong Nueng 12120, Pathumthani, Thailand

3 Thermoelectric Research Laboratory, Center of Excellence on Alternative Energy, Research and Development Institution, Sakon Nakhon Rajabhat University, 680 Nittayo Road, Mueang District, Sakon Nakhon 47000, Thailand

with a *ZT* value of 1.21.[18] Nan et al. reported the use of size-controlled synthesis and transport properties of $Sb_2Te_3$ nanoplates to control the nanoparticle size, and the thickness of the nanoplates was reduced to 80 nm. The high *ZT* was 0.3.[19]

In this work, we have used $Sb_2Te_3$ ink for printing to fabricate $Sb_2Te_3$ films on a $SiO_2$/Si substrate via the screen-printing technique. The screen-printed film thickness was controlled to 200 $\mu$m. The crystal structure, crystallite size, dislocation density, lattice strain, and particle size were studied based on x-ray diffraction (XRD; JSM-7610Fplus) results. The morphology, powder size, and chemical composition of the fabricated films were studied using field-emission scanning electron microscopy (FE-SEM; XRD6100; Shimadzu) and energy-dispersive x-ray spectroscopy (EDS), and the TE properties of the fabricated $Sb_2Te_3$ films after annealing were investigated and are discussed.

## Materials and Methods

### $Sb_2Te_3$ Ink Synthesis

Elemental granules of antimony (Sb), tellurium (Te), and $Sb_2Te_3$ (99.99% purity) were mixed without further purification. Ethylenediamine (>98%), acetonitrile (99.8%), glycerol (99.5%), and ethylene glycol (99.5%) were also used without further purification. Then, the stoichiometric $Sb_2Te_3$ powder was prepared by a planetary ball mill (PM 400) with a rotation speed of 300 rpm for 10, 20, or 30 h to produce small, medium, or large particles, respectively. The resulting powders were then sieved through a shaker for 30 min (with a vibratory sieve shaker; 200 basic). The formation of the $Sb_2Te_3$ powders was confirmed by XRD analysis, as shown in Fig. 1.

$Sb_2Te_3$ ink was prepared by first dissolving 0.32 g of Sb powder and 0.68 g of Te powder in 10 ml of ethylenediamine at room temperature in a fume hood [20,21] and then dissolving it after stirring for 12 h. The solution turned a light purple color. After 40 ml of acetonitrile was added to the mixed solution, the mixture was centrifuged at 3000 rpm for 2 h, after which the precipitated solution was added to a mixed solvent containing 3.6 g of glycerol and 0.4 g of ethylene glycol and stirred for 2 h. A mixture of 4 g of the $Sb_2Te_3$ powder was heated at 453 K for 5 h on a hot plate to thoroughly homogenize the ink.

### Screen-Printing Processing

The $Sb_2Te_3$-ink was screen-printed on a $SiO_2$/Si substrate with a flat painting brush using a screening machine (ZY-TB-B Coater), and the thickness was controlled to 200 $\mu$m.[22] The printed substrates were sequentially dried on a hot plate at 433 K for 30 min and then annealed under vacuum at

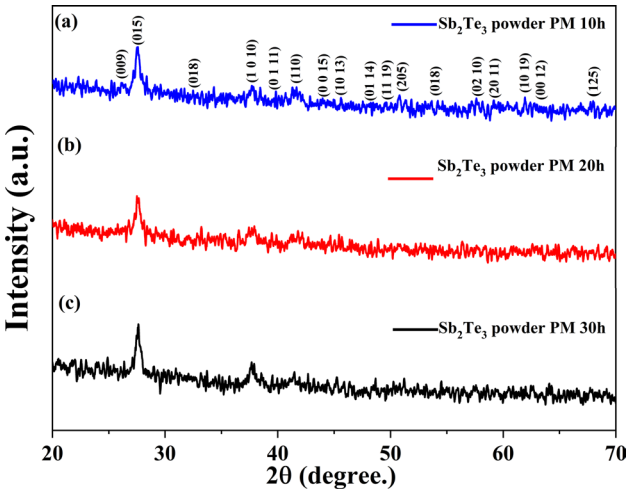


**Fig. 1** XRD patterns of ball-milled $Sb_2Te_3$ powder at 10, 20, and 30 h.

523 K (heating step of 373 K $min^{-1}$) for 30 min (Mini Lamp Annealer Mila5000; Advanced Riko). A schematic of all the processes is shown in Fig. 2.

### Characterization and Measurement

The microstructure of the fabricated films was characterized by FE-SEM operated at 15 kV. XRD patterns were collected using a Cu-$K_{a1}$ x-ray source (wavelength of 1.5418 Å) operating at 40 kV and 40 mA in the range of 20–70° with a scan speed of 5° $min^{-1}$ and a step size of 0.01°. The crystallite size ($D$) of the $Sb_2Te_3$ films was evaluated by Scherrer's equation:

$$D = \frac{K\lambda}{\beta \cos\theta} \tag{1}$$

where $K$ is a dimensionless shape factor (0.9), $\lambda$ is the wavelength of the $CuK_{\alpha 1}$ radiation (1.54186 Å), $\beta$ is the full width at half-maximum (FWHM) of the diffraction peak, and $\theta$ is the Bragg's angle. The dislocation density ($\delta$) and the lattice strain ($\varepsilon$) in the $c$-axis were calculated using[23]:

$$\delta = \frac{1}{D^2} \tag{2}$$

$$\varepsilon = \frac{\beta}{4\tan\theta} \tag{3}$$

Finally, $S$ and $\rho$ were measured at temperatures ranging from 325 K to 525 K using a four-probe method (ZEM-3; Advance Riko). The average size of the films was 3.0 × 15 $mm^2$ on a $SiO_2$/Si substrate, as described previously.[24] The thermal diffusivity $D$ was measured by laser

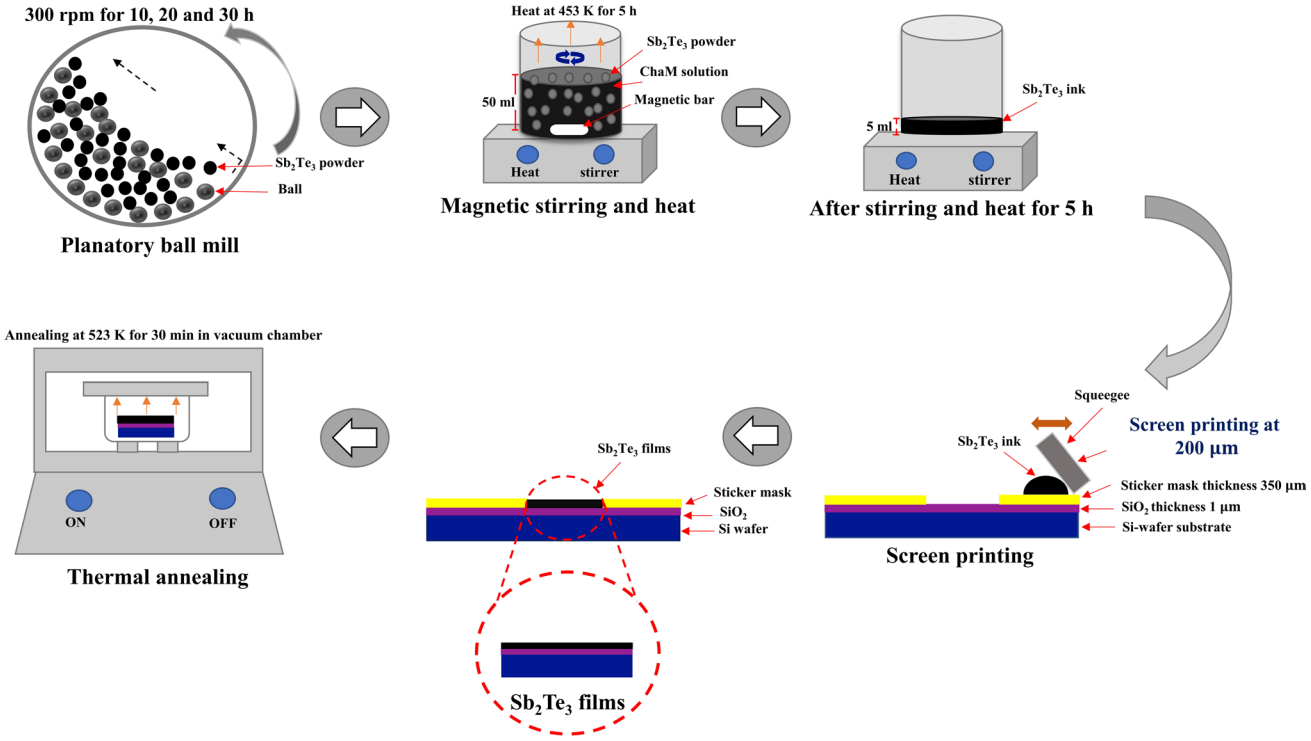


**Fig. 2** Schematic of the screen-printing and thermal-annealing processes.

flash analysis (LFA-457; Netzsch, Germany). The $\kappa$ was calculated from:

$$\kappa = DdC_P \tag{4}$$

The sample density $d$ was determined by the Archimedes method, and the specific heat $C_p$ was measured using a differential scanning calorimeter and the three-line method. The effective average particle size of the $Sb_2Te_3$ films was calculated using[25]:

$$D_{\text{eff}} = 6d_{\text{th}}^{-1}A^{-1} \tag{5}$$

where $d_{\text{th}} = 6.50$ g cm$^{-3}$ and is the theoretical density of $Sb_2Te_3$ and $A$ is the specific surface area.

## Results and Discussion

The XRD patterns of the films of small, medium, and large $Sb_2Te_3$ powders annealed under vacuum at 523 K for 30 min are shown in Fig. 3a. All the XRD pattern peaks correspond to the $Sb_2Te_3$ crystal structure. Therefore, the main peak of the (015) phase at 28° in Fig. 3b corresponds to JCPDS#15-0874 and the rhombohedral structure: $a = b$ 0.4487, and $c = 3.0873$ nm.[26,27] However, the $2\theta$ angle at 28° continuously shifted toward the small-angle side, and the large-angle side showed a highly crystalline structure. The crystallite size, dislocation density, and lattice strain are shown in Table I. The crystallite size of all the films at the (015) plane decreased with increasing particle size.[28] Moreover, the dislocation density and lattice strain increased with increasing particle size, as confirmed by the XRD and SEM results, and these values are affected by the TE PF.[29] In larger particles, carrier-scattering mechanisms, such as impurity scattering, grain boundary scattering, and defect scattering, can be more prominent. These scattering events hinder the movement of the charge carriers, reducing the electrical conductivity and ultimately lowering the PF.

Figure 4 shows the SEM images and average particle sizes of the $Sb_2Te_3$ powders prepared for different durations. The average size of the particles for each sample was calculated by the log-normal distribution function[30]:

$$f(D) = \left(\frac{1}{\sqrt{2\pi\sigma_D}}\right)\exp\left[-\frac{\ln^2\left(\frac{D}{D_0}\right)}{2\sigma^2}\right] \tag{6}$$

where $D$ corresponds to the average powder size and $\sigma_D$ is the standard deviation. The average powder sizes for 10, 20, and 30 h of $Sb_2Te_3$ powder were 3.54, 2.88, and 2.36 $\mu$m, respectively, along with standard deviations of 0.30$\mu$m, 0.25$\mu$m, and 0.23 $\mu$m, respectively. The average size of the

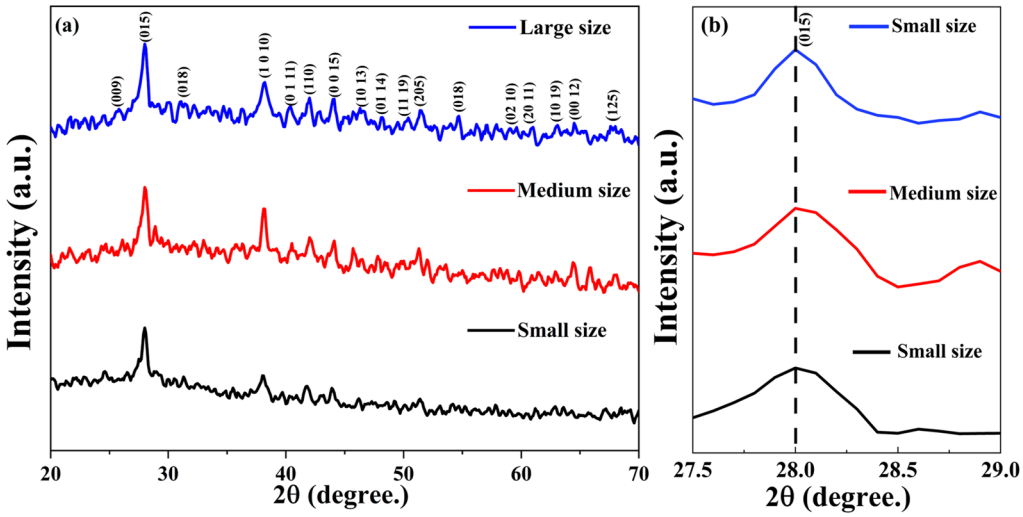


**Fig. 3** XRD patterns of (a) all the peaks and (b) the expansion of the (015) phase for small, medium, and large films.

**Table I** Variation in the crystalline size, dislocation density, lattice strain, and effective average particle size of the films for the different $Sb_2Te_3$ powder sizes

| Sample sizes | $2\theta$ (degrees) | FWHM (015) | D (nm) | $\delta(m^{-2})$ | $\varepsilon(\%)$ | $D_{eff}$ ($\mu$m) |
|---|---|---|---|---|---|---|
| Small | 27.98 | 0.47 | 17.20 | 5.19 | 10.32 | 29.3 |
| Medium | 28.26 | 0.50 | 16.15 | 3.82 | 8.72 | 36.3 |
| Large | 28.00 | 0.58 | 13.87 | 3.37 | 8.33 | 40.4 |

$Sb_2Te_3$ powder decreased after different curing times, as confirmed by the average sizes shown in Fig. 4b, d, and f.

SEM images of the morphology of the top views and cross-sections of the screen-printed $Sb_2Te_3$ films of (a, c) small size, (b, e) medium size, and (c, f) large size are shown in Fig. 5. The final thicknesses of the annealed films were 34 $\mu$m (a), 91 $\mu$m (b), and 184 $\mu$m (c). The annealed films were agglomerated particles due to $\Delta G = \Delta H - TB$, where $\Delta G$ is the change in the free enthalpy, $\Delta H$ is the change in the enthalpy, and $B$ is the Boltzmann entropy.[31] The surface morphology clearly showed the densification of the films during the annealing process. Moreover, the densification of $Sb_2Te_3$ films increased the $B$ value depending on the temperature.[32] However, the particle size of the $Sb_2Te_3$ material and the chemical composition and particle size of the $Sb_2Te_3$ films are predictable PFs. In nanoscale TE materials, when the particle size is comparable to the characteristic length scale of the electrons, a phenomenon called quantum confinement occurs, which leads to discrete energy levels, affecting the electronic structure and transport properties of the material. As a result, the PF can be enhanced due to the increased carrier concentration and improved electrical conductivity.

The chemical composition of the $Sb_2Te_3$ films was confirmed to be Sb and Te by EDS, and the elemental mappings are shown in Fig. 6. The atomic ratios of the Sb:Te films were 34:65, 35:65, and 35:65, as shown in Table II. Therefore, the small powder $Sb_2Te_3$ films have a good ratio of 2:3, because this ratio results in the highest PF. The significant peaks include Sb and Te, indicating the composition of the films, and Si and O are from the $SiO_2$/Si-wafer substrate.[33]

The $S$, $\rho$, and PF of films of small, medium, and large sizes of the $Sb_2Te_3$ powders depend on temperature, as shown in Fig. 7. The obtained $\rho$ values of the films for small, medium, and large films are 0.26, 0.29, and 0.23 m $\Omega$m, respectively, at 515 K. The $\rho$ of all the films decreased with increasing temperature, as shown in Fig. 7a. Moreover, the $\rho$ of all the films decreased with increasing crystallite size, which indicates semiconductor behavior.[34,35] In fact, the $\rho$ of the semiconductor can be determined by:

$$\rho = \frac{1}{ne\mu} \tag{7}$$

where $n$ is the carrier concentration, $e$ is the charging unit, and $\mu$ is the mobility in carrier concentration.[36] Therefore,

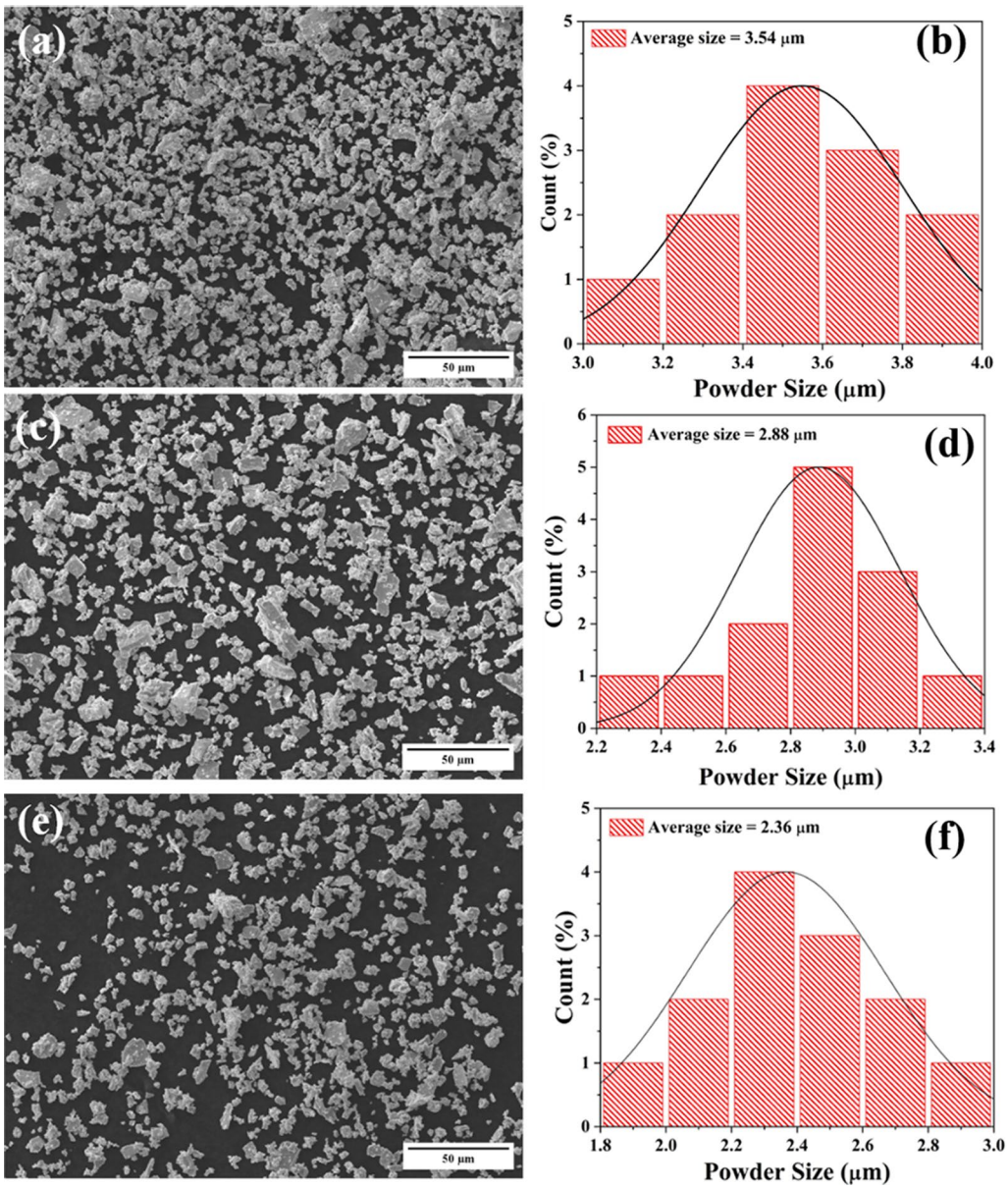


**Fig. 4** SEM images (a, c, e) and powder size distributions (b, d, f) of the $Sb_2Te_3$ powder. Samples were prepared at (a, b) 10, (c, d) 20, and (e, f) 30 h.

the small films had the lowest dislocation density and lattice strain.

The *S* of all the films increased with increasing temperature from 325 K to 425 K and decreased with increasing temperature from 425 K to 525 K, as shown in Fig. 7b. The increased *S* values are due to decreasing carrier concentration, and the decreased values are due to increasing carrier concentration,[37] indicating a change in the TE type. However, all *S* values were positive, indicating *p*-type TE behavior, which decreased with increasing particle size. In fact, the variation in *S* values as a function of the $Sb_2Te_3$ film size is inversely related to the carrier concentration:

$$S(T) = \frac{8\pi^2 k_B^2}{3eh^2} m^* T \left(\frac{\pi}{3n}\right)^{\frac{2}{3}} \tag{8}$$

where $k_B$ is Boltzmann's constant, $h$ is Planck's constant, $m^*$ is the effective mass of the charge carrier, and $n$ is the carrier concentration.[38] The *S* increased with decreasing powder size due to the decrease in carrier concentration. It can be assumed that small grains have a greater density of grain boundaries than medium and large grains, which exhibit high *S* values together with low $\rho$ values, which was confirmed by the SEM images of the surface film.[39] The PF of the small films increases with increasing temperature

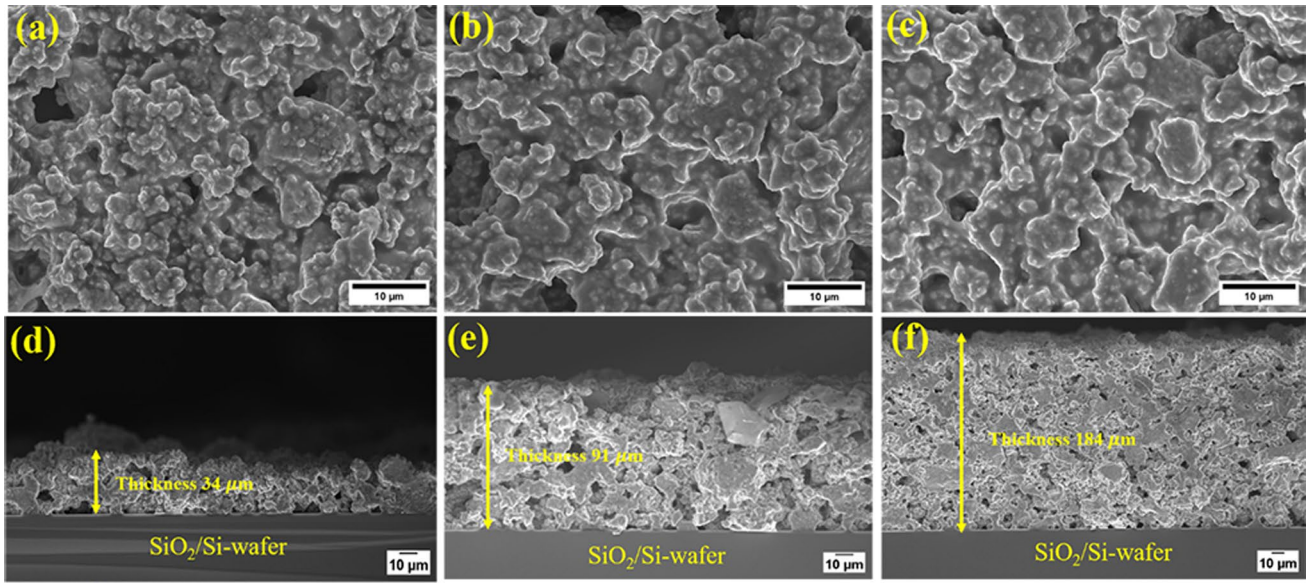


**Fig. 5** SEM images of the surfaces and cross-sections of the (a, d) small, (b, e) medium, and (c, f) large $Sb_2Te_3$ powders.

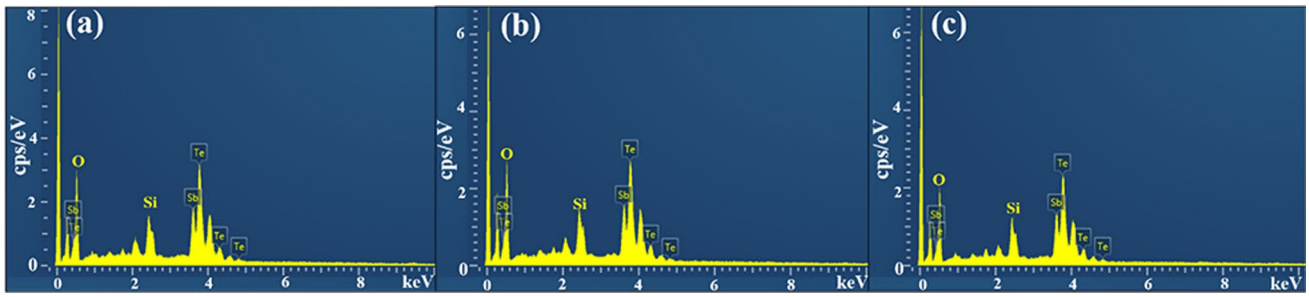


**Fig. 6** EDS spectra and surface maps of (a) small, (b) medium, and (c) large-size $Sb_2Te_3$ films.

**Table II** Atomic ratio and thickness of films of small, medium, and large $Sb_2Te_3$ powders measured by EDS

| Condition | Composition (%) | | Thickness |
|---|---|---|---|
| Films from $Sb_2Te_3$ powder size | Sb | Te | (μm) |
| Small | 34.58 | 65.42 | 34 |
| Medium | 34.78 | 65.22 | 91 |
| Large | 34.95 | 65.05 | 184 |

from 325 K to 425 K and decreases with increasing temperature from 425 K to 525 K, as shown in Fig. 7c. However, the PF of the film increased with increasing temperature from 325 K to 525 K. Therefore, the maximum PF was $11.6 \times 10^{-4}$ W m$^{-1}$ K$^{-2}$ at 425 K. It is important to note that there is an optimal particle size range for maximizing the PF. A too-small particle size may lead to increased phonon scattering, which can detrimentally affect the electrical conductivity. Conversely, excessively large particle sizes may result in increased carrier scattering and reduced PF. Compared with those of bulk TE materials, the $\kappa$ of films of small, medium, and large sizes of $Sb_2Te_3$ powders are significantly lower.[40] These $\kappa$ values are 0.78 W m$^{-1}$ K$^{-2}$, 0.93 W m$^{-1}$ K$^{-2}$, and 1 W m$^{-1}$ K$^{-2}$ at 515 K for small, medium, and large particles, respectively, as shown in Fig. 7d. Consequently, the maximum *ZT* value was achieved for films of small $Sb_2Te_3$ powders, which were 1.04 at 468 K, as shown in Fig. 7e.

## Conclusions

$Sb_2Te_3$ films on $SiO_2$/Si-wafer substrates were fabricated from different particle sizes (small, medium, and large) of $Sb_2Te_3$ powder mixed with ChaM solution for the screen-printing technique, with a fixed thickness of 200 $\mu$m and annealing at 523 K under a vacuum. All the films exhibited

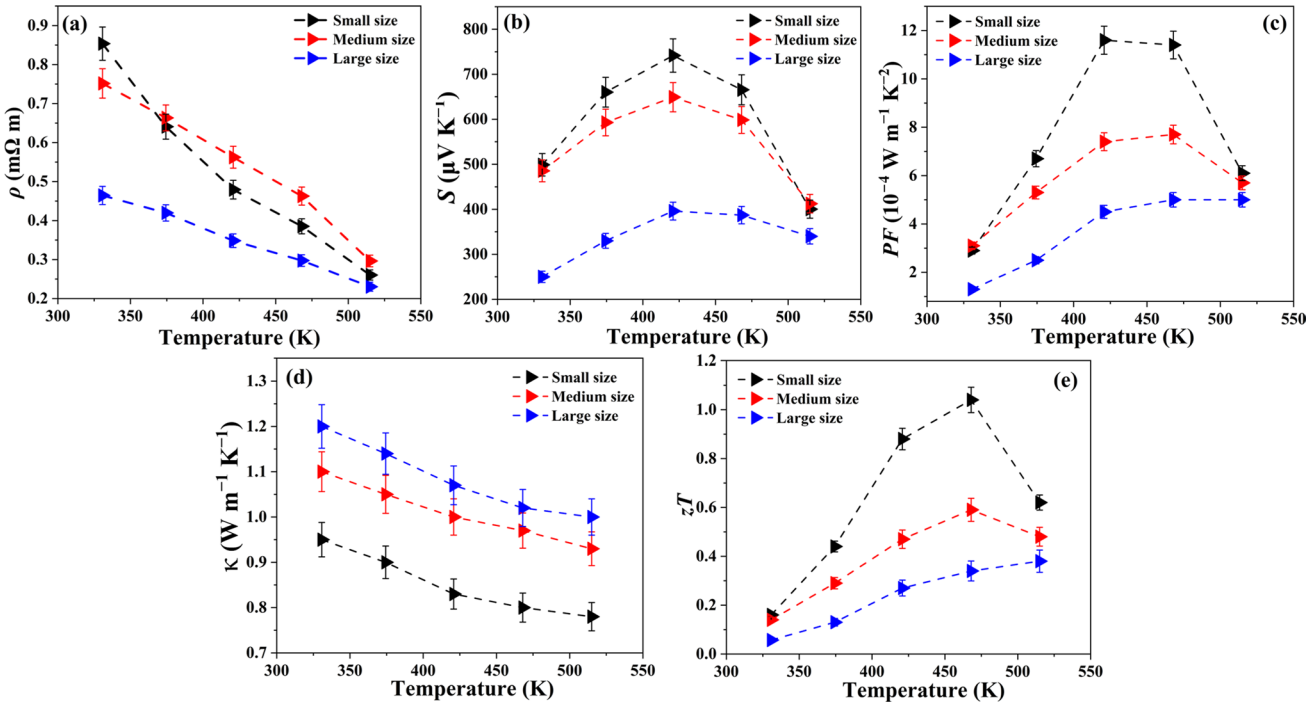


**Fig. 7** Relationships of temperature with respect to (a) $\rho$, (b) $S$, (c) $\kappa$, (d) PF, and (e) $ZT$ for small, medium, and large films.

rhombohedral crystal structures and increased crystallite sizes with increasing particle size after annealing. The effective average particle size of the $Sb_2Te_3$ films increased with increasing powder size. When $\rho$ decreased with increasing temperature, $S$ increased and the PF increased. The maximum $ZT$ was 1.04 at 468 K for the small-size $Sb_2Te_3$ film. Finding the right balance is crucial for optimizing the thermoelectric performance. In some cases, $S$ can increase due to enhanced energy filtering and quantum confinement effects, resulting in improved thermoelectric performance.

**Acknowledgments** This work was supported by the National Science and Technology Development Agency (NSTDA) and Thailand Graduate Institute of Science and Technology (TGIST) Grant, SCA-CO-2563-12020-TH and Program Management Unit for Human Resources & Institutional Development Research and Innovation (PMU-B) e-ASIA JRP program (B16F650001). I would like to express Prof. Ady Suwardi of The National University of Singapore (NUS) for supporting the thermal conductivity measurements.

**Conflict of interest** The authors declare that they have no conflict of interest.

## References

1. Z.B. Zhang, J.Q. Wang, and S. Wang, Roll-to-roll printing of spatial wearable thermoelectrics. *Manuf. Lett.* 21, 28 (2019). https://doi.org/10.1016/j.mfglet.2019.07.002.
2. P.V. Ilaiyaraja, A.C. Sharma, T.K. Dakshinamurthy, and D.C. Sudakar, Fabrication of metal chalcogenide thin films by a facile thermolysis process under air ambient using metal-3-mercaptopropionic acid complex. *Mater. Res. Bull.* 141, 111346 (2021). https://doi.org/10.1016/j.materresbull.2021.111346.
3. S. Bag, P.N. Trikalitis, P.J. Chupas, G.S. Armatas, and M.G. Kanatzidis, Porous semiconducting gels and aerogels from chalcogenide cluster. *Science* 31, 490 (2007). https://doi.org/10.1126/science.11425.
4. S.H. Park, S. Jo, B. Kwon, F. Kim, H.W. Ban, J.E. Lee, D.H. Gu, S.H. Lee, Y. Hwang, J.S. Kim, D.B. Hyun, S. Lee, K.J. Choi, W. Jo, and J.S. Son, High-performance shape-engineerable thermoelectric painting. *Nat. Commun.* 7, 13403 (2016). https://doi.org/10.1038/ncomms13403.
5. H.J. Wu, P.C. Lee, F.Y. Chiu, S.W. Chen, and Y.Y. Chen, Self-assisted nucleation and growth of [010]-oriented $Sb_2Te_3$ whisker: the crystal structure and thermoelectric property. *J. Mater. Chem.* 3, 10488 (2013). https://doi.org/10.1039/C5TC01364J.
6. R. Venkatasubramanian, E. Siivola, T. Colpitts, and B.O. Quinn, Thin-film thermoelectric devices with high room-temperature figures of merit. *Nature* 413, 597 (2001). https://doi.org/10.1038/35098012.
7. K. Park, K. Ahn, J. Cha, S. Lee, S. Chae, I. Cho, I.S.P. Ryee, S. Im, J. Lee, J. Park, S.D. Han, M.J. Chung, and I.T. Hyeon, Extraordinary off-stoichiometric bismuth telluride for enhanced *n*-type thermoelectric power factor. *J. Am. Chem. Soc.* 43, 14458 (2016). https://doi.org/10.1021/jacs.6b09222.
8. S. Thaowonkaew, M. Kumar, and A. Vora-ud, Thermoelectric properties of Ag-doped $Sb_2Te_3$ thin films on $SiO_2$ and polyimide substrate with rapid thermal annealing. *J. Electron. Mater.* 50, 2669 (2021). https://doi.org/10.1007/s11664-021-08788-w.
9. Y.Q. Cao, X.B. Zhao, T.J. Zhu, X.B. Zhang, and J.P. Tu, Syntheses and thermoelectric properties of $Bi_2Te_3/Sb_2Te_3$ bulk nanocomposites with laminated nanostructure. *Appl. Phys. Lett.* 92, 143106 (2008). https://doi.org/10.1063/1.2900960.

10. L. Yang, Z. Gang, M.S. Dargusch, and J. Zou, High performance thermoelectric materials: progress and their application. *Adv. Energy Mater.* 6, 17011797 (2017). https://doi.org/10.1002/aenm.201701797.
11. X. Lu, P. Lu, Y. Fan, W. Zhou, S. Gu, Z. Zhou, J. Zhang, L. Su, L. Wang, and W. Jiang, Structurally nanocrystalline electrically monocrystalline $Sb_2Te_3$ with high thermoelectric performance. *Scr. Mater.* 166, 81 (2019). https://doi.org/10.1016/j.scriptamat.2019.03.013.
12. M. Orrill and S. LeBlance, Printed thermoelectric materials and devices: fabrication techniques, advantages, and challenges. *J. Appl. Polym.* 44256, 1 (2016). https://doi.org/10.1002/app.44256.
13. Y. Zhao, H. Liu, H. Qin, X. Chu, X. Wang, X. Wang, K. Cai, D. Liu, C. Wang, and J. Wang, Spin coating-co-reduction approach: a general strategy for preparation of oriented chalcogenide thin film on arbitrary substrates. *Rare Metals* 30, 651 (2011). https://doi.org/10.1007/s12598-011-0365-z.
14. S.J. Kim, J.H. We, J.S. Kim, G.S. Kim, and B.J. Cho, Thermoelectric properties of *p*-type $Sb_2Te_3$ processed by a screen-printing technique and a subsequent annealing process. *J. Alloys Compd.* 582, 177 (2014). https://doi.org/10.1016/j.jallcom.2013.07.195.
15. R.J. Horwood and T. Better, Understanding of screen print thickness control. *Electron. Sci. Technol.* 1, 129 (1974). https://doi.org/10.1155/APEC.1.129.
16. H. Choi, S.J. Kim, Y. Kim, J.H. We, M. Oh, and B.J. Cho, Enhanced thermoelectric properties of screen-printed $Bi_{0.5}Sb_{1.5}Te_3$ and $Bi_2Te_{2.7}Se_{0.3}$ thick films using a post annealing process with mechanical pressure. *J. Mater. Chem. C.* 5, 8559 (2018). https://doi.org/10.1039/C7TC01797A.
17. F. Kim, B. Kwon, Y. Eom, J.E. Lee, S. Park, S. Jo, S.H. Park, B.S. Kim, H.J. Im, M.H. Lee, T.S. Min, K.T. Kim, H.G. Chae, W.P. King, and J.S. Son, Composition-segmented BiSbTe thermoelectric generator fabricated by multimaterial 3D printing. *Nat. Energy* 3, 301 (2018). https://doi.org/10.1016/j.nanoen.2020.105638.
18. S.H. Park, S. Jo, B. Kwon, F. Kim, H.W. Ban, J.E. Lee, D.H. Gu, S.H. Lee, Y. Hwang, J.S. Kim, D.B. Hyun, S. Lee, K.J. Choi, W. Jo, and J.S. Son, High-performance shape-engineerable thermoelectric painting. *Nat. Commun.* 7, 13403 (2016). https://doi.org/10.1038/ncomms13403.
19. S.J. Kim, J.H. We, and B.J. Cho, A wearable thermoelectric generator fabricated on a glass fabric. *Energy Environ. Sci.* 7, 1959 (2014). https://doi.org/10.1039/C4EE00242C.
20. F. Kim, B. Kwon, Y. Eom, J.E. Lee, S. Park, S. Jo, S.H. Park, B.S. Kim, H.J. Im, M.H. Lee, T.S. Min, K.T. Kim, H.G. Chae, W.P. King, and J.S. Son, 3D printing of shape-conformable thermoelectric materials using all-inorganic $Bi_2Te_3$-based inks. *Nat. Energy* 3, 301 (2018). https://doi.org/10.1038/s41560-017-0071-2.
21. S.K. Wang, T.C. Lin, S.R. Jian, J.Y. Juang, J.S.C. Jang, and J.Y. Tseng, Effects of post-annealing on the structural and nanomechanical properties of Ga-doped ZnO thin films deposited on glass substrate by RF-magnetron sputtering. *Appl. Surf. Sci.* 258, 1261 (2011). https://doi.org/10.1016/j.apsusc.2011.09.088.
22. S.M. Shin, R. Kumar, J.W. Roh, D.S. Ko, H.S. Kim, S.I. Kim, L. Yin, S. Schlossberg, S. Cui, J.M. You, S. Kwon, J. Zheng, J. Wang, and R. Chen, High-performance screen-printed thermoelectric films on fabrics. *Sci. Rep.* 1, 7317 (2017). https://doi.org/10.1038/s41598-017-07654-2.
23. A. Samavati, H. Nur, A.F. Ismail, and Z. Othaman, Radio frequency magnetron sputtered $ZnO/SiO_2$/glass thin film: role of ZnO thickness on structural and optical properties. *J. Alloys Compd.* 671, 170 (2016). https://doi.org/10.1016/j.jallcom.2016.02.099.
24. A. Vora-ud, S. Thaowonkaew, J. Khajonrit, K. Singsoog, P. Muthitamongkol, C. Chananonwathorn, N. Chanlek, M. Horpathum, S. Maensiri, and T. Seetawan, Rapid thermal annealing induced the c-axis (00l) preferred orientation and the *p*-type thermoelectric properties of Bi-Sb-Te thin films. *Thin Solid Films* 706, 138094 (2020). https://doi.org/10.1016/j.tsf.2020.138094.
25. P.M. Radingoana, S.G. Fritsch, J. Noudem, P.A. Olubambi, G. Chevallier, and C. Estournès, Microstructure and thermoelectric properties of Al-doped ZnO ceramic prepared by spark plasma sintering. *J. Eur. Ceram. Soc.* 43, 1009 (2023). https://doi.org/10.1016/j.jeurceramsoc.2022.10.034.
26. G.H. Dong, Y.J. Zhu, and L.D. Chen, Microwave-assisted rapid synthesis of $Sb_2Te_3$ nanosheets and thermoelectric properties of bulk samples prepared by spark plasma sintering. *J. Mater. Chem.* 10, 1976 (2010). https://doi.org/10.1039/B915107A.
27. T. Chen, P. Fan, Z. Zheng, D. Zhang, X. Cai, G. Liang, and Z. Cail, Influence of substrate temperature on structural and thermoelectric properties of antimony telluride thin films fabricated by RF and DC co-sputtering. *J. Electron. Mater.* 41, 679 (2012). https://doi.org/10.1007/s11664-011-1896-2.
28. J.B. Thorat, S.V. Mohite, S.B. Madake, S.K. Shinde, D.S. Lee, J. Jung, K.Y. Rajpure, T.J. Shinde, V.J. Fulari, and N.S. Shinde, Physico-electrochemical investigation of electrodeposited nanocrystalline $Sb_2Te_3$ thin films. *Int. J. Res. Anal. Rev.* 1269, 2349 (2021). https://doi.org/10.1039/C5TC03656A.
29. P. Junlabhut, P. Nuthongkum, A. Harnwunggmoung, P. Limsuwan, C. Hatayothai, R. Sakdanuphab, and A. Sakulkalavek, Thickness dependence of thermoelectric properties and maximum output power of single planar $Sb_2Te_3$ films. *Materials* 15, 8850 (2022). https://doi.org/10.3390/ma15248850.
30. H. Jalili, B. Aslibeiki, A.G. Varzaneh, and V.A. Chernenko, The effect of magneto-crystalline anisotropy on the properties of hard and soft magnetic ferrite nanoparticles. *Beilstein J. Nanotechnol.* 10, 1348 (2019). https://doi.org/10.3762/bjnano.10.133.
31. D. Vollath, Criteria ruling particle agglomeration. *Beilstein J. Nanotechnol.* 12, 1093 (2021). https://doi.org/10.3762/bjnano.12.81.
32. R.M. German, Rheological model for viscous flow densification during supersolidus liquid phase sintering. *Sci. Sinter.* 38, 27 (2006). https://doi.org/10.2298/SOS0601027G.
33. P. Bathnagar, and D. Vashaee, Development of MEMS process compatible $(Bi, Sb)_2(Se, Te)_3$-based thin films for scalable fabrication of planar micro-thermoelectric generators. *Micromachines* 13, 1459 (2022). https://doi.org/10.3390/mi13091459.
34. M.H. Lee, K.R. Kim, J.S. Rhyee, S.D. Park, and G.J. Snyder, High thermoelectric figure-of-merit in $Sb_2Te_3/Ag_2Te$ bulk composites as Pb-free *p*-type thermoelectric materials. *J. Mater. Chem. C* 3, 10494 (2015). https://doi.org/10.1039/C5TC01623A.
35. E. Vieira, J. Figureira, A.L. Pires, J. Grilo, M.F. Silva, A.M. Pereira, and L.M. Goncalves, $Bi_2Te_3$ and $Sb_2Te_3$ thin films with enhanced thermoelectric properties for flexible thermal sensors. *Proceedings* 2, 815 (2018). https://doi.org/10.3390/proceedings2130815.
36. G.J. Snyder, A.H. Snyder, M. Wood, R. Guranathan, B.H. Snydera, and C. Niu, Weighted mobility. *Adv. Mater.* 32, 2001537 (2020). https://doi.org/10.1002/adma.202001537.
37. S. Kumar, M. Faraz, and N. Khare, Enhanced thermoelectric properties of $Sb_2Te_3$-graphene nanocomposite. *Mater. Res. Express* 6, 085079 (2019). https://doi.org/10.1088/2053-1591/ab1d1f.
38. T.H. An, Y.S. Lim, M.J. Park, J.Y. Tak, S. Lee, H.K. Cho, J.Y. Cho, C. Park, and W.S. Seo, Composition-dependent charge transport and temperature-dependent density of state effective mass interpreted by temperature-normalized pisarenko plot in $Bi_{2-x}Sb_xTe_3$ compounds. *Appl Mater.* 4, 104812 (2016). https://doi.org/10.1063/1.4961106.
39. P. Dharmaiah, H.S. Kim, C.H. Lee, and S.J. Hong, Influence of powder size on thermoelectric properties of p-type25%$Bi_2Te_3$-75%$Sb_2Te_3$ alloys fabricated using gas-atomization and

spark-plasma sintering. *J. Alloys Compd.* 686, 1 (2016). https://doi.org/10.1016/j.jallcom.2016.05.340.
40. S.M. Yoon, B. Madavali, C.H. Lee, O.E. Femi, J.H. Lee, S.H. Song, and S.J. Hong, Fabrication of large-scale *p*-type 75% $Sb_2Te_3$-25% $Bi_2Te_3$ thermoelectric materials by gas atomization and hot isostatic pressing. *Mater. Res. Bull.* 130, 110924 (2020). https://doi.org/10.1016/j.materresbull.2020.110924.